Science and Technology Indonesia
e-ISSN:2580-4391 *p*-ISSN:2580-4405
Vol. 10, No. 3, July 2025

Research Paper

Synthesis and Characterization of $TiO_2/CaTiO_3$ Perovskite Composite Derived from *Pinctada maxima* Shell Waste

Dian W. Kurniawidi[1*], Susi Rahayu[1], Arif Budianto[1], Kormil Saputra[1], Wida Puteri Agista[2,3], Thatit Suprayogi[4], Resti Marlina[5]

[1]*Physics Study Program, Universitas Mataram, Mataram, West Nusa Tenggara, 83115, Indonesia*
[2]*Magister Physics Study Program, Universitas Negeri Malang, Malang, East Java, 65145, Indonesia*
[3]*Tinta Emas Institute, Mataram, West Nusa Tenggara, 83115, Indonesia*
[4]*Physics Study Program, Universitas Palangkaraya, Palangka Raya, Central Kalimantan, 74874, Indonesia*
[5]*Research Center for Biomass and Bioproducts National Research and Innovation Agency (BRIN), West Java, 16911, Indonesia*
***Corresponding author**: diankurnia@unram.ac.id

Abstract
This study has succeeded in synthesizing and characterizing $TiO_2/CaTiO_3$ perovskite composites using calcium carbonate ($CaCO_3$) from shellfish waste (*Pinctada maxima*). Synthesis was carried out through the coprecipitation method with variations in the molar ratio of $CaCO_3$:TiO_2 and calcination temperatures (700°C, 800°C, and 900°C). Characterization was carried out using FTIR, DTA-TG, XRD, SEM-EDS, BET and UV-Vis. The results of the analysis showed that the calcination temperature affected the powder color, crystal structure, thermal properties and particle size. The DTA-TG analysis shows that increasing the calcination temperature up to 900°C significantly reduces mass loss to 51.88%, with minimal thermal events, indicating the formation of a thermally stable and well-crystallized $TiO_2/CaTiO_3$ structure. At a temperature of 900°C, a more perfect $CaTiO_3$ was formed with the whitest powder color, the anatase and brookite phases of TiO_2 were still detected, while the calcite phase was still found at a temperature of 700°C. The morphology of the samples showed agglomeration with increasingly uniform particle sizes at higher calcination temperatures. Complementary BET analysis confirms that the composite possesses a mesoporous structure with a specific surface area of 11.42 m^2/g and a pore size distribution of 3-5 nm, making it suitable for adsorption and photocatalytic applications. UV-Vis analysis showed an increase in the band gap value along with the increase in the TiO_2 ratio. This is also confirmed by the presence of Urbach energy which tends to increase with increasing TiO_2 ratio.

Keywords
$CaCO_3$, $TiO_2/CaTiO_3$, Calcination, Perovskite, Band Gap

Received: 9 April 2025, Accepted: 10 June 2025
https://doi.org/10.26554/sti.2025.10.3.924-942

1. INTRODUCTION

Research on the use of solar cells as an energy source continues to develop until now. This development is marked by the presence of generations of solar cell technology ranging from the first generation, second generation, to the third generation. The use of silica material as the basic structure of solar cells is the first generation. Silica-based solar cells have the advantage of producing high efficiency, but require high costs (Thomas et al., 2025). While the second generation solar cells are thin-layer-based solar cells. The technique of applying this thin layer does not require high costs in the production process. However, the cadnium content in the thin layer can cause air pollution (Song et al., 2022). The weaknesses of the two generations are overcome through the emergence of third-generation solar cells. Renewable solar cells are classified into organic solar cells which have an efficiency of 8%, DSSC (Dye Sensitized Solar Cell) with an efficiency of ~11% and Perovskite Solar Cell (PSC) which has an efficiency of ~19.3% with cheaper fabrication costs compared to dye-sensitized solar cells (Aftabuzzaman et al., 2020; Giannouli, 2021).

One of the parameters that affect the efficiency of solar cells is the selection of active materials in solar cells. The ideal material as an active material is a material that has optimal optical properties. Optimization of maximum photon absorbance capability and a small energy band gap is highly desired. These characteristics are usually possessed by semiconductor materials. The principle of semiconductor materials is to absorb photon energy from sunlight. Then when the photon energy is greater than the band gap energy, it will cause electrons to be excited from the valence band to the conduction band (Ezat et al., 2021). Meanwhile, in terms of optical properties, per-

ovskite materials have a stronger optical absorption mechanism compared to the first and second generations because they have direct band gap energy that affects the absorbance capacity. Perovskite materials have many types, one of which is perovskite material from calcium titanate ($CaTiO_3$) (Attou et al., 2022). $CaTiO_3$ can be obtained by synthesizing basic materials in the form of calcium carbonate ($CaCO_3$) with titanium oxide (TiO_2).

$CaCO_3$ is found in abundance in limestone, marine animal shells, one of which is pearl shells. Pearl oyster cultivation is quite developed on the island of Lombok, which has caused the accumulation of pearl oyster shell waste. Based on the explanation above, the use of waste as a source of smart material for New and Renewable Energy (EBT) is very important. In addition to the abundance of raw materials, the high demand for this energy has encouraged the development of perovskite smart materials on the island of Lombok. The manufacture of perovskite materials has been carried out by previous researchers.

Although research on the manufacture of perovskite materials, especially $CaTiO_3$, has been carried out previously, most of these studies are still focused on the use of synthetic raw materials or limited mineral sources (Cerón-Urbano et al., 2023; Lalan et al., 2022; Singh et al., 2024). Research that relies on organic waste, such as pearl oyster shells, as a source of calcium carbonate for perovskite synthesis is relatively small (Beuvier et al., 2022; Dassouki et al., 2023). This opens up opportunities to explore the potential of abundant pearl oyster waste on the island of Lombok as an alternative raw material that is more environmentally friendly and economical. In addition, although various applications of renewable energy have been widely explored, the integration of locally sourced perovskite materials such as these is still rarely discussed in the context of efficient and sustainable use of renewable energy (Handayana et al., 2022; Kurniawidi et al., 2022; Widiastuti et al., 2023).

However, one of the main challenges in the synthesis of perovskite materials, especially $TiO_2/CaTiO_3$ composites, is the production process which still requires high temperatures, strict morphology control, and the use of pure chemicals at relatively expensive costs (Hamzah and Nababan, 2011; Kurniawidi et al., 2022). This complexity is an obstacle in the commercialization and widespread application of perovskite materials, especially in areas with limited access to synthetic materials. In this context, pearl oyster shell waste (*Pinctada maxima*) which is abundantly available on Lombok Island with an estimated 600 tons per year offers the potential as an alternative source of $CaCO_3$ that is economical and environmentally friendly (Kurniawidi et al., 2024). Previous studies in other countries have also shown the use of marine biominerals, such as oyster shells in China and the Philippines, as a basic calcium material for energy and environmental applications (Chilakala et al., 2019; Hamzah and Nababan, 2011).

These results indicate that local biominerals can be processed through calcination to produce CaO suitable for use in the synthesis of $CaTiO_3$. By utilizing local natural resources, this study aims to develop more economical and sustainable materials for large-scale applications. Therefore, the development of perovskite research from pearl oyster shells needs to be explored more deeply to support the renewable energy sector of West Nusa Tenggara, especially Lombok Island.

2. EXPERIMENTAL SECTION

2.1 Materials

The materials used in this study include Pearl oyster shell waste (*Pinctada maxima*) which has been mechanically ground to produce $CaCO_3$ powder with a mesh of 100. The details of the procedure are explained in the next sub-chapter. The next materials are TiO_2 Pa 98% powder, Aquades, Phenolphthalein (PP) indicator, NaOH 0.25 M, HCl 0.50 M, 70% Alcohol, Ethanol P.a 98%, and EtOH 99% with the Merck brand, India.

2.2 Preparation of Calcium Carbonate ($CaCO_3$) Powder

The process of making $CaCO_3$ from pearl oyster shells consists of three main stages, namely cleaning, size modification, and testing the $CaCO_3$ content following the Kandiah et al. (2023) procedure. First, cleaning is done by washing the shells using a brush, rinsing with alcohol, then drying them in direct sunlight. Second, size modification is done by breaking the shells to make them smaller, then calcining them in a furnace at a temperature of 500°C for 2 hours. The calcination results are ground using a mortar and sieved with a size of 100 mesh to obtain a homogeneous powder. Testing the CaCO3 content is done by acid-base titration. A total of 5 grams of $CaCO_3$ powder is dissolved in 50 mL of 0.50 M HCl, then heated for 10 minutes with a blank solution (50 mL of 0.50 M HCl). After cooling, the solution is filtered, then the filtrate and blank are diluted to 100 mL. Each solution is taken 10 mL, added 2 drops of PP indicator, then titrated with 0.25 M NaOH until the color changes to purplish pink. The volume of NaOH used was recorded for $CaCO_3$ content analysis. Preparation details can be seen in Figure 1.

2.3 Synthesis of $TiO_2/CaTiO_3$ Perovskite Composite

$TiO_2/CaTiO_3$ perovskite composites were synthesized using a modified coprecipitation method inspired by previous studies Han et al. (2017). Initially, a molar ratio of $CaCO_3$:TiO_2 = 1:7 was selected based on preliminary screening for producing a CaTiO3-rich composite with enhanced photocatalytic activity, as higher TiO_2 content is often associated with improved light absorption and electron mobility in perovskite structures (Cesconeto et al., 2018). In this synthesis, $CaCO_3$ was dissolved in 100 mL of distilled water, while TiO_2 was dispersed in 100 mL of 98% ethanol. Both solutions were magnetically stirred for 2 hours until homogeneous. The mixture was then precipitated, washed several times with distilled water to remove impurities, and dried in an oven at 100°C for 2 hours. The resulting powder was ground and calcined at three different temperatures (700°C, 800°C, and 900°C) for 3 hours to evaluate the optimal thermal conditions for crystallization.

© 2025 The Authors.

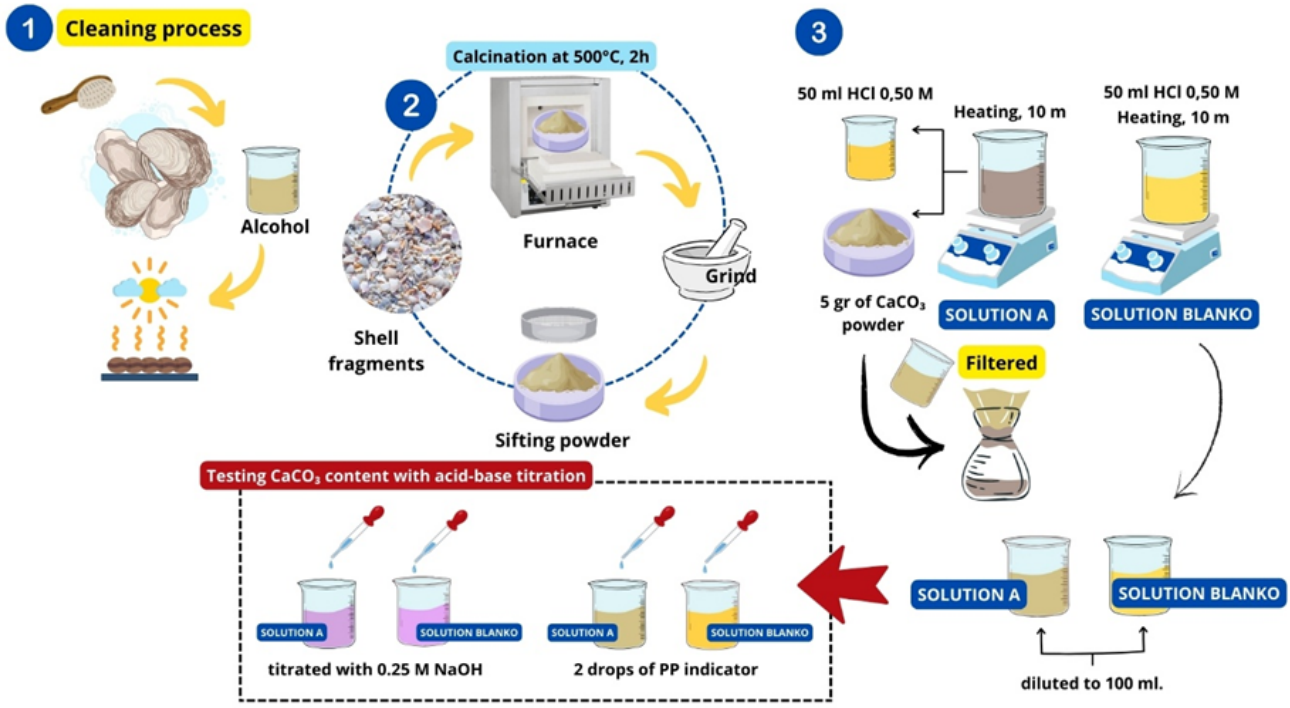

Figure 1. Illustration of Preparation of Calcium Carbonate ($CaCO_3$) Powder

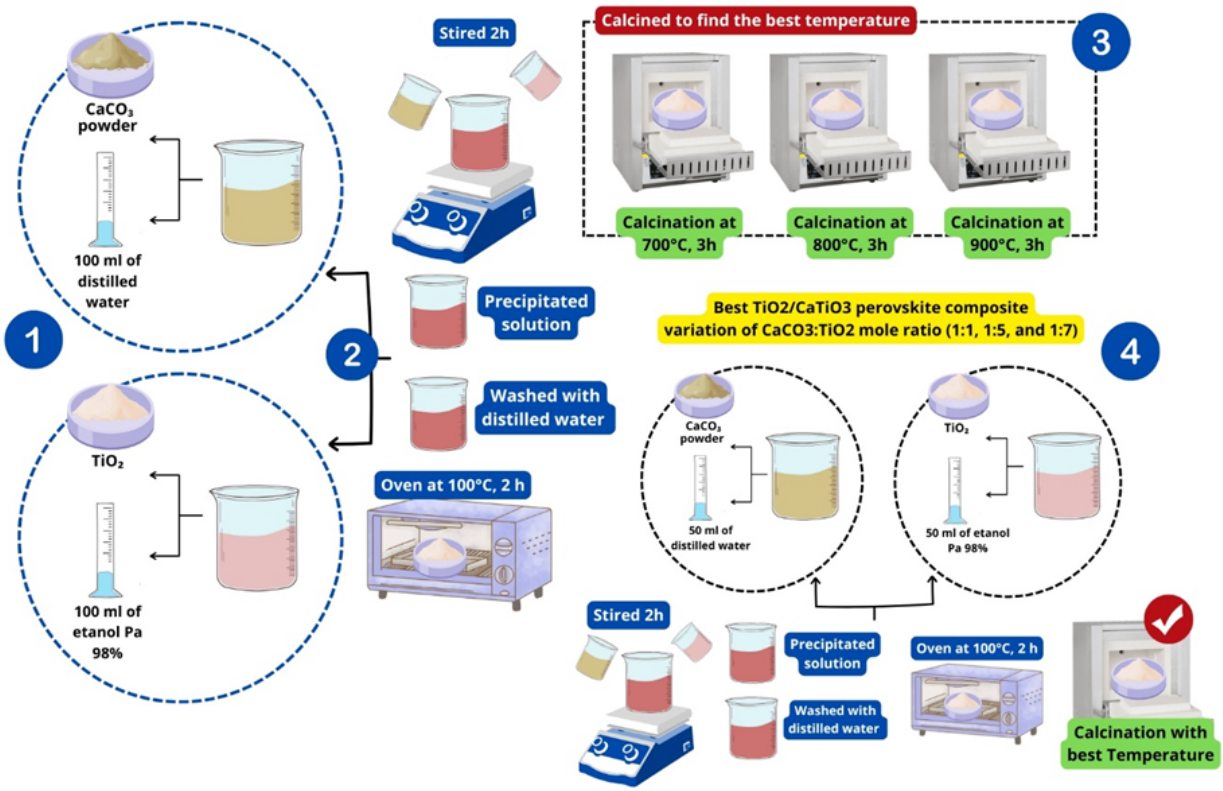

Figure 2. Illustration of Synthesis of $TiO_2/CaTiO_3$ Perovskite Composite

© 2025 The Authors.

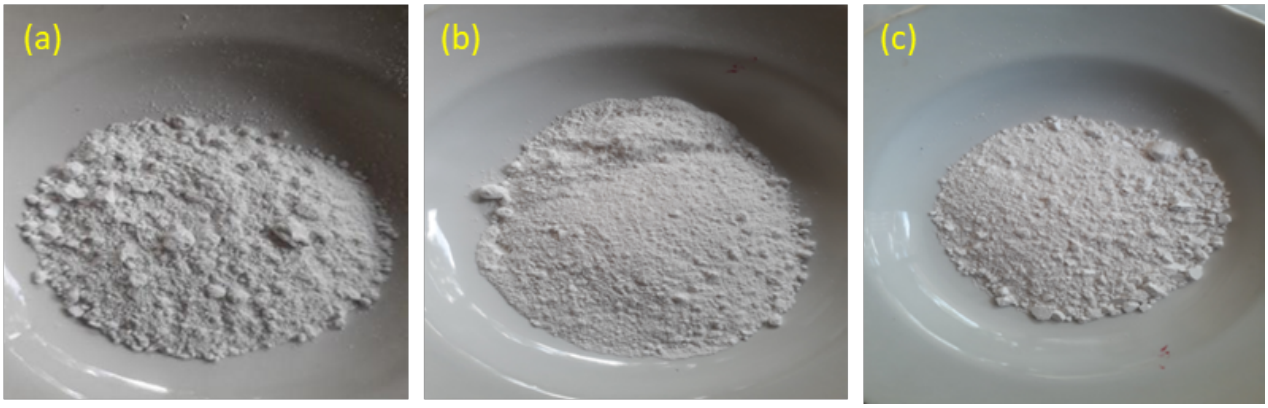

Figure 3. Results of $TiO_2/CaTiO_3$ Synthesis with Variations in Calcination Temperature (a) 700°C (b) 800°C and (c) 900°C

Table 1. FTIR Analysis Results of $TiO_2/CaTiO_3$ Perovskite Composites

Wavenumber				Functional Group
Ref	700°C	800°C	900°C	
3600-3000 (Kandiah et al., 2023)	3467.26	3467.21	3467.26	O – H Stretching
1626 (Diningsih and Rohmawati, 2022)	1650.71	1650.92	1650.71	O−H Stretching
1423 (Kandiah et al., 2023)	1422.43	-	-	C−O Stretching
700-400 (Saputra et al., 2024)	688.25	679.52	678.98	Ti−O Stretching
573-420 (Singh et al., 2024)	571.48	563.51	567.99	Ca−O Stretching

The calcined powders were sieved using a 100-mesh sieve and stored for characterization.

Characterization was carried out using Fourier Transform Infrared Spectroscopy (FTIR; Shimadzu IRPrestige-21), Differential Thermal Analysis-Thermogravimetry (DTA-TG, NETZSCH TG209 F1 Libra) and X-Ray Diffraction (XRD; PANalytical X'Pert ^{3} Powder, Netherlands). Based on the best crystallinity and bonding characteristics observed from FTIR and XRD results, the optimal calcination temperature was selected for the second stage of synthesis. To evaluate the effect of precursor composition, the composite was resynthesized at the selected calcination temperature using mole ratios of CaCO3:TiO2 = 1:1, 1:5, and 1:7.

These ratios were chosen to represent a broad variation in TiO_2 content from stoichiometric (1:1), sub-stoichiometric (1:5), to TiO_2-rich (1:7) in order to study its influence on optical, morphological, and structural properties of the composite. Ratios such as 1:3, 1:9, or 1:10 were not used in this work to maintain a manageable experimental scope and focus on ratios that show contrasting but representative behaviors based on related literature (Ferrari et al., 2019; Liu et al., 2019). Further investigation of other ratios is suggested for future studies. In this second synthesis step, weighed amounts of $CaCO_3$ and TiO_2 were prepared according to the stoichiometry of each ratio. $CaCO_3$ was dissolved in 50 mL of distilled water, and TiO_2 was dispersed in 50 mL of ethanol. Both suspensions were stirred using a magnetic stirrer until a homogeneous slurry was obtained, followed by precipitation, filtration, and three-step washing with distilled water. The resulting slurry was dried at 100°C and then calcined at the previously determined optimal temperature. Final samples were characterized using SEM-EDS (JEOL JCM-7000, Japan), Brunauer-Emmett-Teller (BET, Quantachrome Nova 4200e), and Ultraviolet-Visible (UV-Vis) Spectroscopy (Orion Aquamate 8000). Synthesis steps and flow are schematically illustrated in Figure 2.

2.4 Characterization of $TiO_2/CaTiO_3$ Perovskite Composite

$TiO_2/CaTiO_3$ perovskite composite particles that have been in powder form with a calcination temperature variation of 700°C-900°C were characterized and analyzed using an FTIR instrument to determine the functional groups formed using and the vibration modes formed. DTA-TG to analyzing the thermal properties of both weight change and heat flow as a function of temperature. In addition, an XRD test was carried out at an angle of 2θ with a range of 10°-90° to determine the crystal phase formed. The analysis of the $TiO_2/CaTiO_3$ perovskite composite phase is based on COD 2310710 for the anatase phase, AMCSD 0005160 for the brokit phase, COD 9002801 for the $CaTiO_3$ phase, and COD 9000965 for the calcite phase ($CaCO_3$). The phase formation is based on refinement using the Rietveld method assisted by rietica software and as a comparative measurement is carried out using the Debye-Scherrer method. Furthermore, the best $TiO_2/CaTiO_3$ perovskite composite that has been resynthesized with variations

© 2025 The Authors.

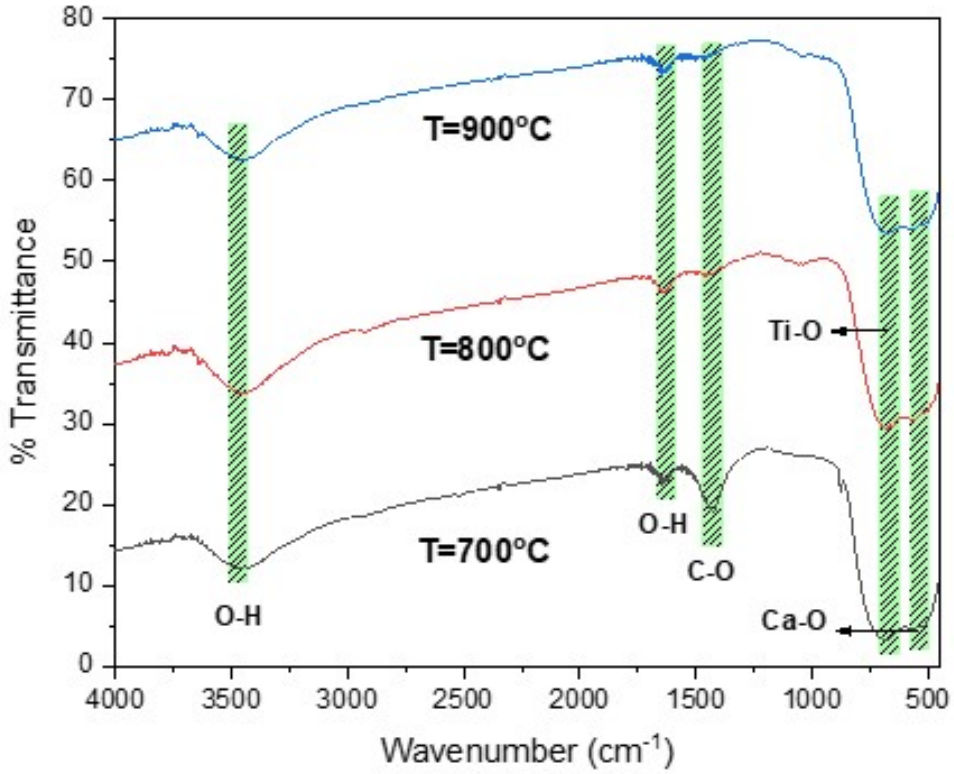

Figure 4. FTIR Test Spectra of $TiO_2/CaTiO_3$ Perovskite Composite with Calcination Temperatures of 700°C, 800°C and 900°C

of $CaCO_3$:TiO_2 (1:1, 1:5, and 1:7) is viewed for morphology, constituent elements, area mapping, and particle size distribution using SEM-EDS, BET to measure the specific surface area of powder. Then the absorption test was carried out using UV-vis and the energy gap calculation was based on the Tauc transformation equation.

3. RESULTS AND DISCUSSION

3.1 Cross Section of $TiO_2/CaTiO_3$ Perovskite Composite and Functional Group Analysis

The manufacture of perovskite composites ($TiO_2/CaTiO_3$) has been successfully carried out using calcium carbonate ($CaCO_3$) sourced from *Pinctada maxima* shell waste. The $CaCO_3$ compound produced is predominantly grayish white. The results can be seen in Figure 3.

The white powder in Figure 3 indicates that the $TiO_2/CaTiO_3$ based perovskite composite has been successfully synthesized. Of the three samples of the synthesis results, there is a slight difference in the color obtained, namely the $CaTiO_3$ perovskite sample with a calcination temperature of 900°C produces the whitest color, while the samples at calcination temperatures of 800°C and 700°C produce a grayish white color. This is according to Ezat et al. (2021) that $CaTiO_3$ begins to form at temperatures above 800°C, while temperatures below it are not significant. Furthermore, an analysis was carried out related to the functional groups formed from the $TiO_2/CaTiO_3$ perovskite composite using FTIR. Samples with variations in calcination temperature were first finely ground before FTIR testing was carried out, this was intended so that the results of the IR transmittance spectrum of the $TiO_2/CaTiO_3$ perovskite composite obtained were clearer. The FTIR test results for the $TiO_2/CaTiO_3$ perovskite composite with variations in calcination temperature are shown in Figure 4.

Based on Figure 4, it is known that there are 5 major functional groups formed including: Ca−O,Ti−O,C−O, and O−H. From all the functional groups, it states that the $TiO_2/CaTiO_3$ perovskite composite has been formed based on the functional groups, only in the C−O functional group there is a fairly deep valley at a calcination temperature of 700°C which indicates that there is still raw material in the form of $CaCO_3$ formed. More details of the results can be seen in Table 1.

Based on Table 1 the wave numbers formed in the $TiO_2/CaTiO_3$ perovskite composite, the experimental results show almost the same results as the wave numbers in the literature. The results of the FTIR test show that, in all three samples, $CaTiO_3$ perovskite has been formed, which can be shown in the resulting wave numbers, where the formation of the $TiO_2/CaTiO_3$ perovskite composite is marked by the emergence of functional groups with Ca−O stretching mode vibrations that occur at 571 cm^{-1} - 567 cm^{-1}. Of the three samples, the most different is in the $TiO_2/CaTiO_3$ perovskite composite sample with a calcination temperature of 700°C, namely that

© 2025 The Authors.

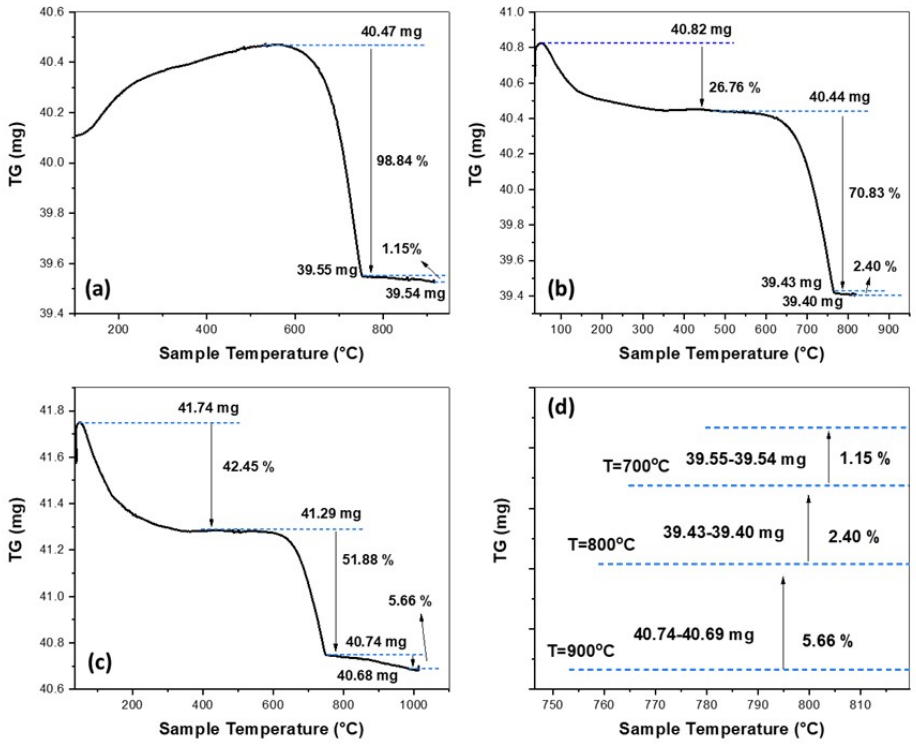

Figure 5. (a)TGA Curve of Samples With Variations of 700°C, (b) 800°C, (c) 900°C, (d) Difference in Percentage Increase in Mass Loss

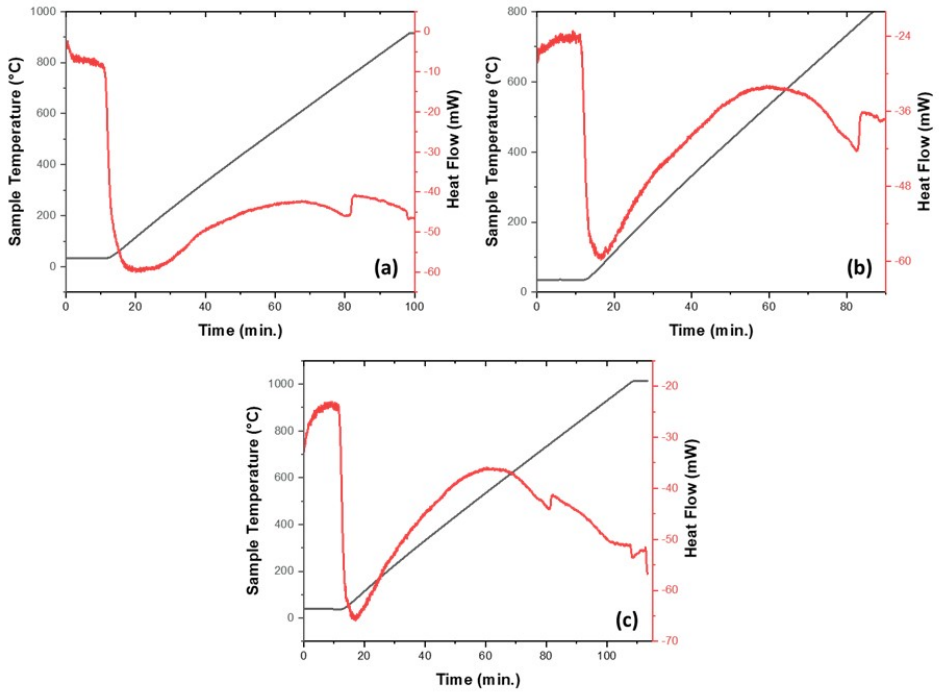

Figure 6. DTA Curves of Samples with Temperature Variations (a) 700°C, (b) 800°C, and 900°C

© 2025 The Authors.

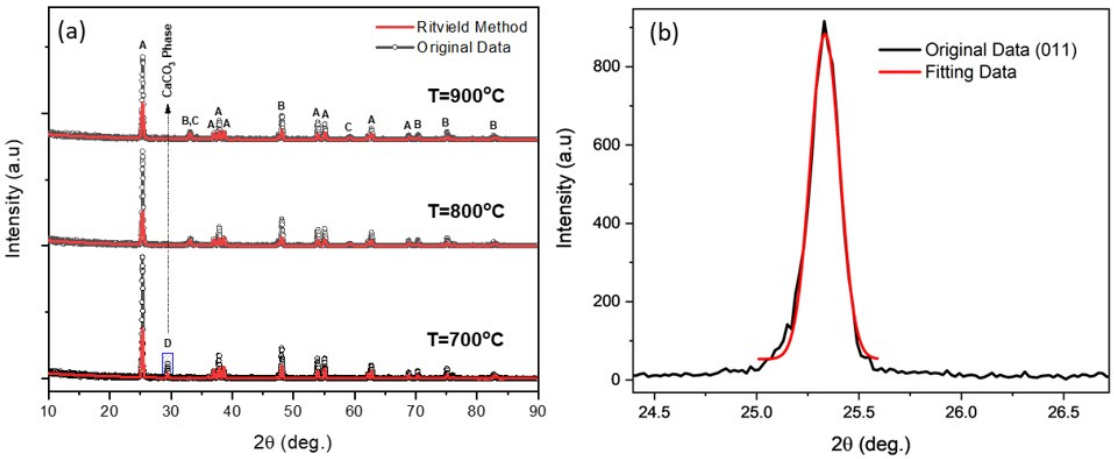

Figure 7. XRD Pattern of $CaTiO_3$ with Variations in Calcination Temperature that has Been (a) Refined using the Rietveld Method and Debye Scherrer Fitting Results of $CaTiO_3$ at Peak (110) variation 700°C

Table 2. Number of Phases Formed, 2 Specific Theta and Position of the Hkl Plan

Phase Code	2 Theta (deg.)			Peak Position of Hkl)	
	700°C	800°C	900°C	700°C	800°C & 900°C
A (Anatase)	25.46	25.54	25.38		[011]
	37.02	36.84	36.93		[220]
	37.96	39.18	39.18		[004]
	38.77	41.29	41.29		[103]
	53. 79	54.02	54.02		[015]
	55.12	55.17	55.19		[131]
	62.37	62.44	62.78		[024]
	68.88	68.88	68.76		[116]
	-	32.96	33.36	-	[112]
B (Brokite)	48.18	48.13	48.13		[020]
	70.49	69.14	70.11		[040]
	75.20	75.33	75.35		[432]
	82.86	82.76	82.77		[305]
C ($CaTiO_3$)	-	59.11	59.20	-	[204]
D ($CaCO_3$)	29.35	-	-	[104]	-

there is a C−O stretch at a wave number of 1422.43 cm^{-1} which indicates that there is still carbon content, either from raw material or residual carbon dioxide (CO_2) that has not been completely decomposed during the calcination process of the $CaTiO_3$ sample using a temperature of 700°C.

The FTIR test results also provide information on functional groups with a Ca−Ti−O stretching mode indicating the formation of a TiO_2/$CaTiO_3$ perovskite composite. It can be seen that the wave absorption spectra are not too sharp, indicating that the crystallinity formed in the $CaTiO_3$ perovskite sample has a crystallinity that is not too high. Of the three $CaTiO_3$ perovskite samples with variations in calcination temperature, it can be seen that the peak in the Ca−Ti−O functional group with a calcination temperature of 900°C has a sharper spectrum. This indicates that the sample with a calcination temperature of 900°C has higher crystallinity. To prove the results obtained in the FTIR test, namely that the $CaTiO_3$ perovskite structure has been formed, further testing was carried out using XRD.

3.2 DTA-TGA Curve Analysis Results for TiO_2/$CaTiO_3$ Perovskite Composite

Next, an analysis was carried out on the TiO_2/$CaTiO_3$ perovskite composite samples TGA curve, the results of which can be seen in Figure 5. Figure 5 shows TGA curves of TiO_2/$CaTiO3_3$ composites calcined at 700°C, 800°C, 900°C, while

© 2025 The Authors.

Table 3. Results of Lattice Parameter Analysis, Phase Percentage and Crystal Structure

Sample	Lattice Constant a (Å)	b (Å)	c (Å)	% Phase	Structure
700°C					
Anatase	3.7842	3.7842	9.507	42.03	Tetragonal
Brokite	11.4786	5.352	4.6135	54.69	Orthorhombic
$CaTiO_3$	5.316	5.316	7.7704	2.94	
$CaCO_3$	4.9809	4.9809	17.0452	0.34	Trigonal (Hex.)
800°C					
Anatase	3.78220	3.78220	9.50460	15.82	Tetragonal
Brokite	15.43400	3.80800	4.46980	78.53	Orthorhombic
$CaTiO_3$	5.37770	5.42930	7.65400	5.65	
900°C					
Anatase	3.7818	3.7818	9.5016	48.80	Tetragonal
Brokite	11.4313	4.399	9.3915	32.07	Orthorhombic
$CaTiO_3$	5.3876	5.4195	6.6468	19.13	

Figure 6 presents the corresponding DTA (Differential Thermal Analysis) profiles. Together, these results illustrate the thermal decomposition behavior, phase transformation, and structural evolution of the materials. In Figure 6(a), the sample calcined at 700°C shows the highest mass loss of approximately 98.84%, with three major stages of decomposition. The first stage, occurring around 50–200°C, corresponds to the evaporation of physically adsorbed water and hydroxyl groups, indicated by an endothermic peak in the DTA curve Figure 6(a). The second stage, within 200-400°C, shows continued mass loss likely due to the thermal decomposition of organic residues, such as citric acid or nitrate complexes used during sol-gel synthesis. This is accompanied by a broader endothermic trough, confirming that decomposition absorbs thermal energy. The third mass loss, visible in the 400–600°C range, is marked by a weak exothermic peak in the DTA, which suggests the initial formation of crystalline oxide phases, potentially involving $CaTiO_3$ nucleation. However, the high overall mass loss suggests that the material remains thermally unstable and contains undecomposed precursors, particularly $CaCO_3$, which is known to decompose fully above 700°C.

For the 800°C sample Figure 5(b), the total mass loss is lower, around 70.83%, and the TGA curve shows a more stabilized profile after ~500°C. In Figure 6(b), the DTA reveals a clear exothermic peak around 580-620°C, corresponding to the crystallization of $CaTiO_3$ perovskite phase. The reduced intensity of earlier endothermic events compared to the 700°C sample indicates that most volatiles and organics were already removed during the calcination process. The exothermic behavior at this stage reflects the rearrangement of cations (Ca^{2+} and Ti^{4+}) into a more ordered oxide structure, releasing energy during lattice formation (Tanos et al., 2024). In Figure 5(c), the 900°C sample exhibits the lowest mass loss at 51.88%, indicating that the material has undergone complete thermal treatment, with minimal residuals. The DTA curve in Figure 6(c) confirms this with a nearly flat profile, showing only a minor exothermic shoulder around 600°C, which may reflect final crystallite growth or densification. The absence of major endothermic or exothermic features suggests that the structure is already crystallized and thermally stable, consistent with the formation of pure $CaTiO_3$ and TiO_2 (anatase or rutile) phases.

As shown in Figure 5(d), the trend of decreasing total mass loss with increasing calcination temperature aligns with previous studies. Mishra et al. (2024a) reported that elevated temperatures enhance the complete decomposition of organics and promote crystalline phase development in metal oxide systems. Wendari et al. (2024) further observed that major mass loss in sol-gel derived perovskites typically occurs below 400°C due to organic breakdown, while crystallization and thermal stabilization become prominent beyond 800°C. These trends are also supported by the shifting and decreasing intensity of exothermic peaks in the DTA curves, which reflect the progressive crystallization and solid-state reaction of $CaTiO_3$ lattice as calcination temperature increases.

Based on Figure 6(a), the DTA curve for the 700°C sample shows a strong endothermic peak in the range of 50-200°C, indicating the evaporation of physically adsorbed water and possible dehydroxylation. A broader endothermic region appears between 200-400°C, associated with the thermal decomposition of residual organic matter, including citric acid or nitrates from the sol-gel synthesis route. At around 600°C, a small exothermic peak is observed, suggesting the onset of crystallization or solid-state reaction leading to the formation of intermediate oxide phases, likely involving Ti and Ca species. In Figure 6(b) for the 800°C sample, the initial endothermic effect due to moisture loss is still present but with lower intensity, indicating reduced adsorbed water content. Notably, a stronger exothermic event appears around 580–620°C, likely related to the formation of crystalline $CaTiO_3$ perovskite phase, as the sample at this stage transitions from an amorphous or

© 2025 The Authors.

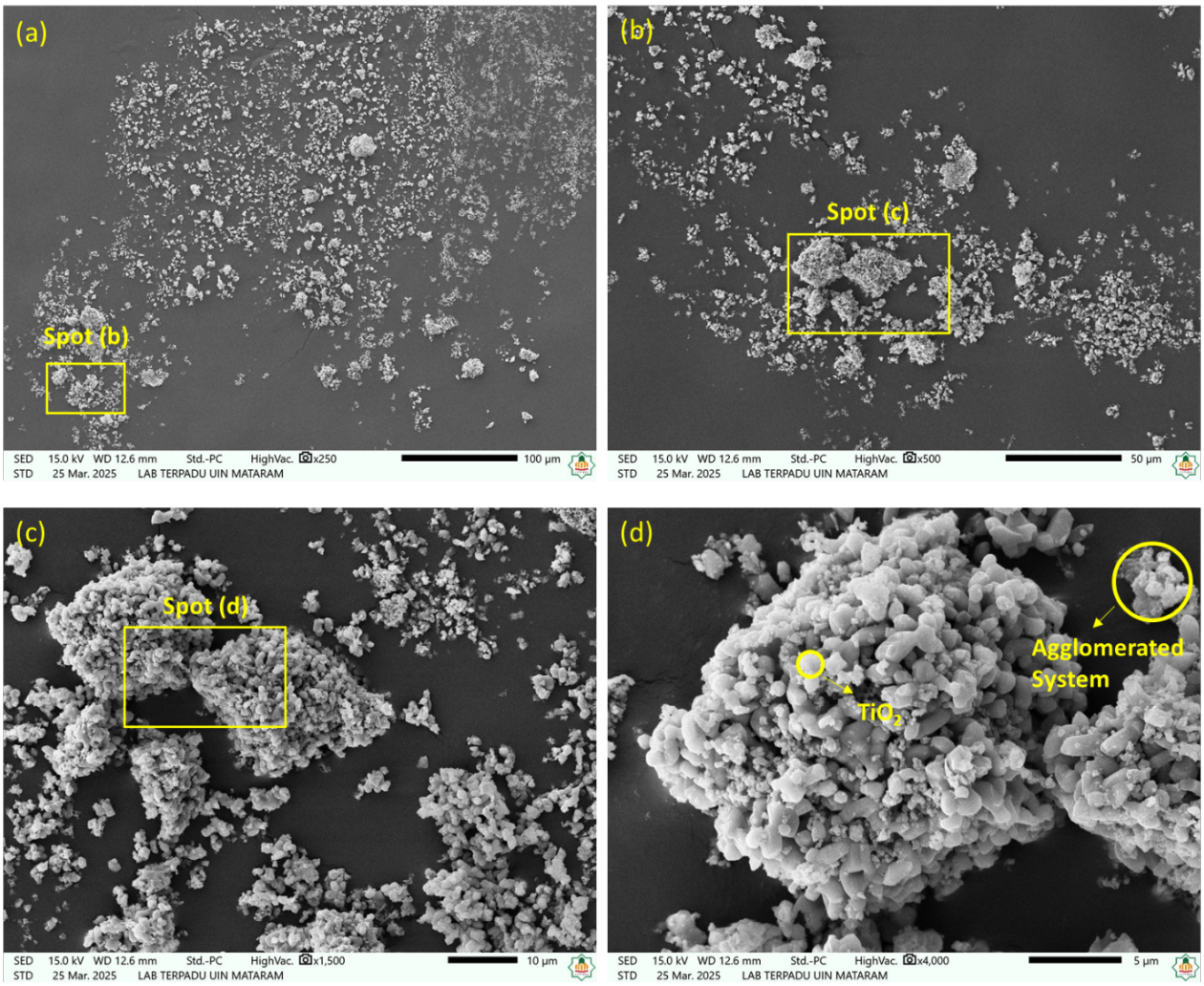

Figure 8. Morphology of $TiO_2/CaTiO_3$ perovskite at 900°C Calcination Temperature

Table 4. Differences in Crystal Size, Cell Volume, Molecular Weight, and Density

Sample	Crystallite Size (nm)		Volume Cell (Å^3)	MW (g/mol)	ρ (g/cm^3)
	Rietveld	Debye-Scherrer			
Anatase	87.5		136.14	2044.8	24.93
Brokite	3.97	74.02	359.12	639.2	2.95
$CaTiO_3$	84.6		222.3	959.8	7.16
$CaCO_3$	63.6		366.19	4140.3	18.76
800◦C					
Anatase	108.8		136.14	2044.8	24.93
Brokite	2.62	54.28	301.64	639.2	3.51
$CaTiO_3$	99.3		222.3	959.8	7.16
900◦C					
Anatase	156.23		135.90	2044.8	24.97
Brokite	2	45.23	252.25	639.2	1.39
$CaTiO_3$	133.99		223.24	959.8	7.13

© 2025 The Authors.

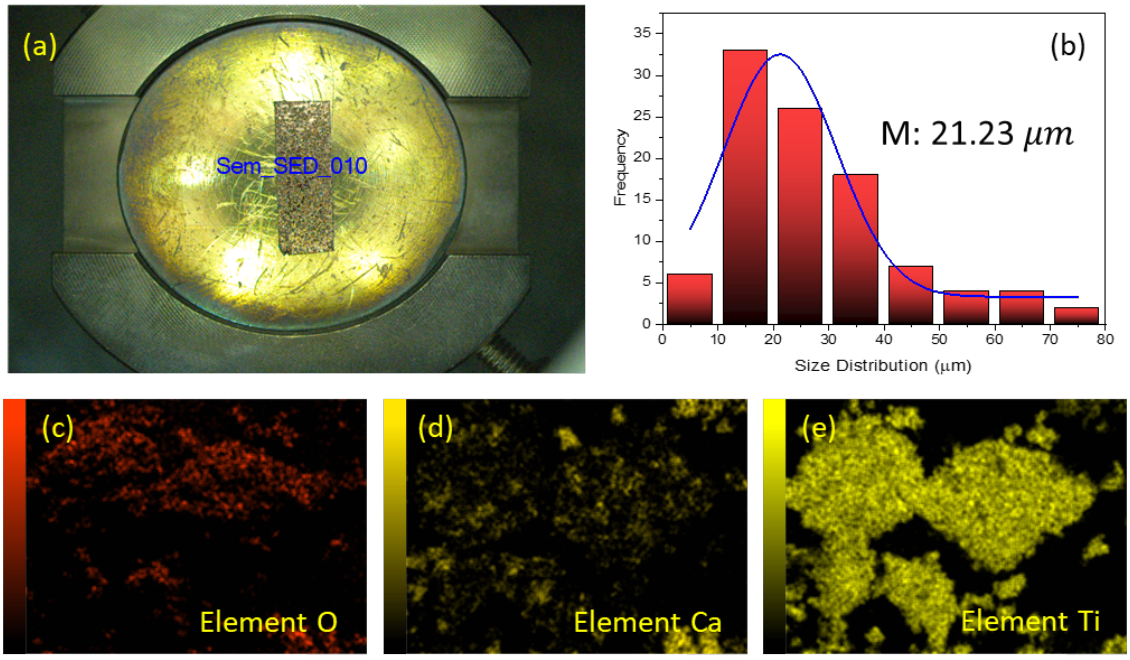

Figure 9. Particle Size Distribution and Mapping of $TiO_2/CaTiO_3$ with 900°C Calcination

semi-crystalline to a more ordered structure.

The thermal behavior suggests that some transformation processes are still occurring at this temperature. Figure 6(c) shows the DTA curve of the 900°C sample. The curve reveals a much smoother profile, with weaker endothermic and exothermic signals compared to the lower-temperature samples. The minor exothermic peak around 600°C may correspond to the final stage of crystallization or densification. The overall flatness of the DTA curve beyond this point indicates that the material has reached a thermodynamically stable crystalline phase, with minimal further transformation occurring during heating. The gradual reduction in the intensity and number of thermal events from 700°C to 900°C supports the conclusion that higher calcination temperatures promote more complete thermal decomposition and crystallization. These findings align with those of Jabbarzare (2022) and Li et al. (2024), who reported that increased calcination temperatures reduce residual organics and enhance the formation of perovskite and oxide phases in metal-oxide composites, as evidenced by the flattening of DTA curves at elevated temperatures.

3.3 Crystal Structure Analysis of $TiO_2/CaTiO_3$ Perovskite Composite

The synthesized $TiO_2/CaTiO_3$ perovskite composite samples were further characterized using X-ray Diffraction (XRD). The diffractogram pattern of the $TiO_2/CaTiO_3$ perovskite composite is shown in Figure 7. Based on the diffraction pattern, several crystalline phases were identified, including the TiO_2 phase in the form of anatase and brookite, and the $CaTiO_3$ phase (COD 9002801) (Saputra et al., 2024). In addition, the presence of the calcite phase ($CaCO_3$) (COD 9000965) originating from the initial raw material was still detected, even though it had gone through a calcination process at a temperature of 700°C. The existence of a diffraction peak from $CaCO_3$ at a temperature of 700°C can be explained based on the kinetics of calcite thermal decomposition. In general, the decomposition of $CaCO_3$ to calcium oxide (CaO) and carbon dioxide (CO_2) occurs in several stages, with the initial decomposition temperature ranging from 600-700°C, depending on factors such as particle size, heating atmosphere, and partial pressure of CO_2 in the heating environment. Previous studies have shown that in an open atmosphere or under conditions of high partial pressure of CO_2, the decomposition of $CaCO_3$ to CaO can be delayed until higher temperatures, even approaching 800-900°C.

In addition, the rate of $CaCO_3$ decomposition also depends greatly on the morphology and crystallinity of the initial material. If the calcite particles have a larger size or a more stable crystal structure, the decomposition process will be slower, so that some $CaCO_3$ can still be detected in the XRD pattern even though it has been calcined at 700°C. This is well confirmed in Table 4 which shows the large size of anatase which hinders the decomposition of $CaCO_3$. Furthermore, an analysis of the diffraction peaks was carried out using the Rietveld and Debye-Scherrer methods to determine various parameters such as crystal size, density, molecular weight, lattice constant and hkl plane formed. The results of the analysis can be seen in Table 2, Table 3, and Table 4. Based on Figure 7a, there is a main peak, namely (110) from anatase. In addition, there are other peaks that are also characteristic of the brokite phase, and

© 2025 The Authors.

$CaTiO_3$. In addition, peak (110) was fitted using the Gaussian equation to obtain the FWHM value which was then input to obtain the crystallite size shown in Table 2.

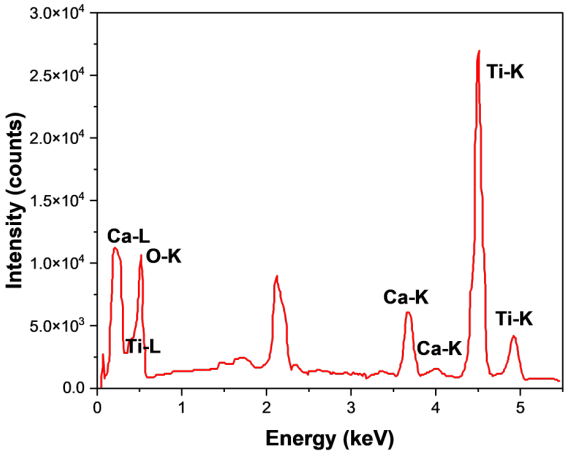

Figure 10. Results of EDS Spectrum of $TiO_2/CaTiO_3$ and Analysis of Elemental Composition

Table 5. Majority Element Composition of $TiO_2/CaTiO_3$ Perovskite Composites

Element	Mass %	Atom %
O	34.30 ± 0.70	60.68 ± 1.23
Ca	4.39 ± 0.11	3.10 ± 0.08
Ti	61.30 ± 0.52	36.22 ± 0.31
Total	100.00	100.00

Table 2 shows that there are eight peaks and hkl planes formed from the anatase phase including [011], [220], [004], [103], [015], [131], [024] and [116]. This phase is the most dominant phase of the formed sample. The emergence of the anatase phase is caused by several aspects, especially the temperature used. Furthermore, there are 5 hkl planes formed from brokite including [112], [020], [040], [432], and [305]. Then the phases of $CaTiO_3$ and calcite each produce one peak. Based on these peaks, a peak growth path is obtained on the [204] plane which begins to be detected at a calcination temperature of 800°C and the disappearance of the [112] peak or calcite phase. These results also confirm both previous studies which state that $CaTiO_3$ begins to appear and is stable at temperatures above 800°C (Cerón-Urbano et al., 2023). Furthermore, the results of the lattice parameter analysis, phase percentage and structure of the $TiO_2/CaTiO_3$ perovskite composite can be seen in Table 3.

Based on the analysis results in Table 3, several important findings were obtained related to the evolution of the crystalline phase in the $TiO_2/CaTiO_3$ perovskite composite. At a temperature of 700°C, the two main phases of TiO_2 formed were anatase (42.03%) and brookite (54.69%), with anatase having a tetragonal structure and brookite being orthorhombic. With increasing temperature to 800°C, the percentage of anatase decreased drastically to 15.82%, while brookite increased significantly to 78.53%. At 900°C, the anatase fraction increased again to 48.80%, while brookite decreased to 32.07%. This pattern indicates the existence of a transformation between TiO_2 phases, which can be attributed to the kinetics of crystal growth and the thermal stability of each phase. Previous studies have shown that anatase tends to transform into the rutile phase at temperatures above 700-800°C, although under certain conditions, brookite can remain stable at higher temperatures (Cerón-Urbano et al., 2023; Sen et al., 2022). The $CaTiO_3$ phase begins to form at a temperature of 700oC with a very small percentage (2.94%). At 800°C, the $CaTiO_3$ content increases to 5.65%, and reaches 19.13% at 900°C. This indicates that the reaction between $CaCO_3$ and TiO_2 in forming $CaTiO_3$ intensifies as the temperature increases.

Research by Altin (2023) shows that the synthesis of $CaTiO_3$ generally occurs at temperatures of 800-1000°C, where high temperatures are needed to allow sufficient ionic diffusion to form a stable perovskite structure. At 700°C, a small amount of $CaCO_3$ phase (0.34%) was still detected, indicating that the thermal decomposition of calcite had not yet fully occurred. This is in line with the results of a study Diningsih and Rohmawati (2022), which stated that the calcination of $CaCO_3$ generally begins at a temperature of 600-700°C, but under certain conditions, especially if there is interaction with other materials, decomposition can be delayed to 800-900°C. Basically, the lattice parameters for all phases show changes with increasing calcination temperature. In the $CaTiO_3$ phase, for example, there is a significant change in the lattice parameters, with the c value decreasing from 7.7704 Å(700°C) to 7.654 Å(800°C) and 6.6468 Å(900°C). This decrease can be attributed to the increase in crystallinity and densification of the structure due to the effects of high temperature (Liu et al., 2019). Next, calculations were made regarding the Crystal Size formed, Cell Volume, Molecular Weight (MW), and Density (ρ), the results of which can be seen in Table 4.

From Table 4, it can be seen that the crystallite size increases with increasing calcination temperature. At 700°C, the crystallite size of anatase based on the Rietveld method is 87.5 nm, while at 900°C it increases to 156.23 nm. The same thing also happens to $CaTiO_3$, which was initially 84.6 nm at 700°C and increased to 133.99 nm at 900°C. Meanwhile, the brookite phase experienced a decrease in crystallite size from 3.97 nm at 700°C to only 2 nm at 900°C, indicating that this phase is increasingly unstable at high temperatures. The unit cell volume is relatively stable for $CaTiO_3$, ranging around 222–223 Å3, while for anatase it remains at 2044.8 Å3. However, the cell volume of brookite decreased drastically from 359.12 Å3 at 700°C to 252.25 Å3 at 900°C, which may indicate a phase transformation or increase in material density. The density (ρ) also showed an interesting trend, with anatase

© 2025 The Authors.

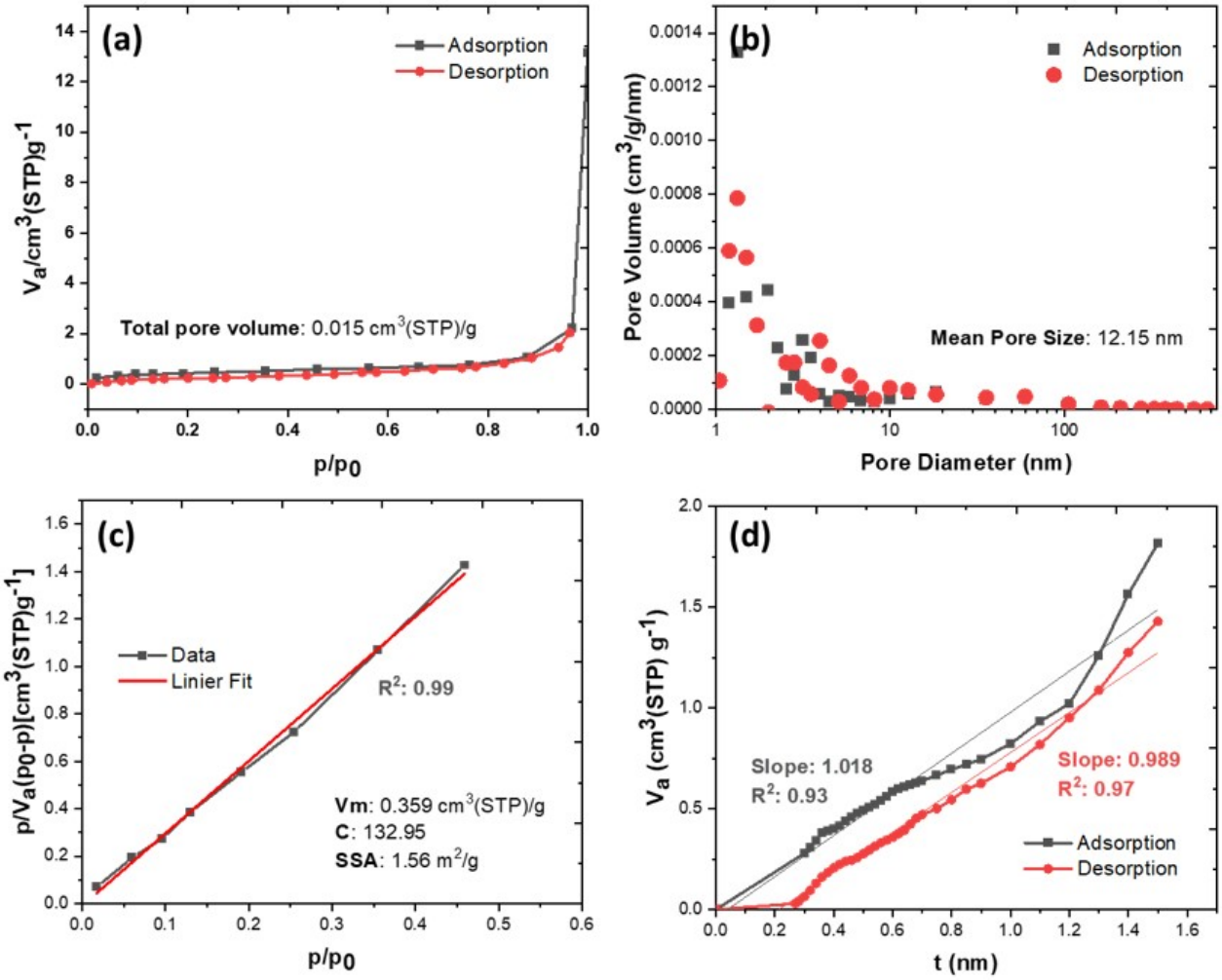

Figure 11. BET Characterization Results of $TiO_2/CaTiO_3$ Perovskite Composites with 900°C Calcination

remaining at around 24.9 g/cm^3, $CaTiO_3$ at around 7.1 g/cm^3, but brookite decreased drastically from 2.95 g/cm^3 to 1.39 g/cm^3.

This result is consistent with previous studies showing that anatase undergoes significant crystal growth with increasing calcination temperature, which is caused by the increase in thermal energy facilitating atomic diffusion and grain coalescence. For example, a study by Vasconcelos et al. (2021) also found that anatase begins to experience a significant increase in crystal size above 700°C and can undergo transformation into rutile phase above 900°C. In addition, a study by Li et al. (2022) showed that brookite tends to be unstable at high temperatures and undergoes conversion to anatase or rutile phases, which may explain the drastic decrease in its crystallite size in this study. For $CaTiO_3$, these results support the findings of Jiang et al. (2024) who reported that the crystallite size increased with increasing calcination temperature, but the cell volume remained relatively constant.

This indicates that crystal growth is more dominant than changes in crystal structure. The stability of the $CaTiO_3$ cell volume can also be attributed to the nature of perovskite which has a stable crystal structure over a wide temperature range. The calcite phase was only detected at 700°C with a crystallite size of 56.6 nm and no longer appeared at higher temperatures. This confirms that $CaCO_3$ undergoes thermal decomposition at temperatures above 700°C, which is in accordance with previous studies by Altin (2023) that calcite begins to decompose into CaO and CO_2 at temperatures around 600–700°C, and is usually no longer detected at 800°C or higher in an open system. The decomposition of $CaCO_3$ that occurred in this study also shows that the synthesis environment used allows good CO_2 release, so that at temperatures of 800°C and 900°C no residual $CaCO_3$ was detected. The results of the XRD test concluded that the best $TiO_2/CaTiO_3$ perovskite composite

© 2025 The Authors.

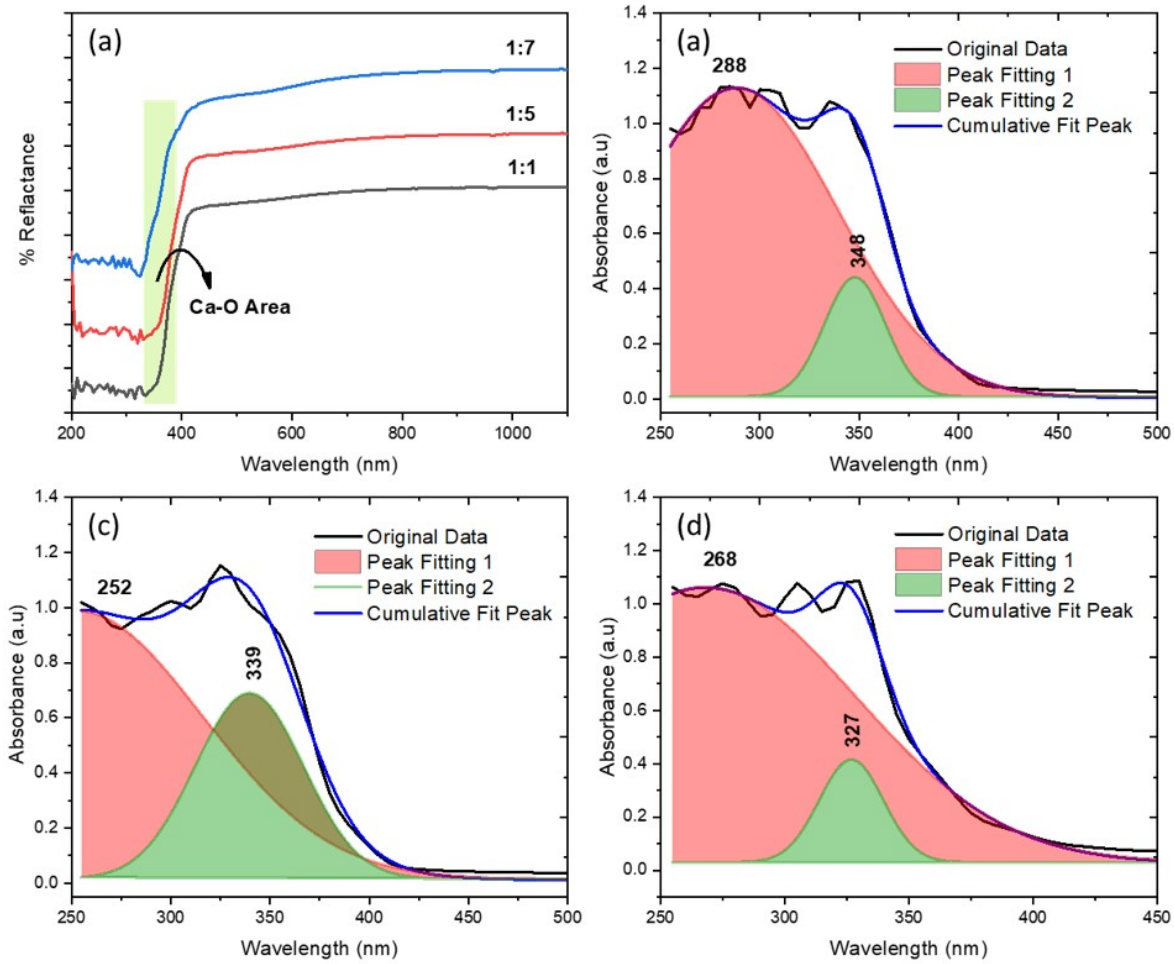

Figure 12. Graph of UV-VIS Characterization Results of $TiO_2/CaTiO_3$ with Variations in Mass Comparison of TiO_2 and $CaCO_3$ (1:1, 1:5 and 1:7) (a) Reflectance, and (b-d) Absorbance

was found at a calcination temperature of 900°C.

3.4 Morphological Analysis, Particle Size Distribution, Mapping, and Porosity Analysis of $TiO_2/CaTiO_3$ Perovskite Composites

The $TiO_2/CaTiO_3$ perovskite composite sample with a calcination temperature of 900°C was further characterized using SEM-EDX, the results of which can be seen in Figure 8. Figure 8(a) and Figure 8(b) at 250× and 500× magnifications show an uneven particle distribution, with areas showing agglomeration of particles of varying sizes. It is also known that the $TiO_2/CaTiO_3$ perovskite formed resembles a granule mass. Research by Mishra et al. (2024b) showed that at high calcination temperatures, the growth of $CaTiO_3$ crystallites tends to occur non-uniformly, which causes particle clustering due to the sintering effect. Figure 8(c) at 1,500× magnification shows the particle structure in higher detail, where it is seen that nanoparticles begin to gather to form larger aggregates. Kaabi et al. (2023) reported that the synthesis of TiO_2 via the sol-gel method often produces structures that undergo agglomeration due to sintering at high temperatures. Figure 8(d) at 4,000× magnification shows a clearer agglomeration system, with small grains merging to form larger structures. The point marked as TiO_2 indicates that the majority of visible particles are TiO_2 that surround the pores of $CaTiO_3$. The large size of $CaTiO_3$ chunks allows TiO_2 with brokite and anatase phases to adhere more strongly. This result is also supported by the particle size distribution and element mapping shown in Figure 9.

Figure 9 shows the characterization of $TiO_2/CaTiO_3$ material after calcination at 900°C, including particle size distribution and mapping of major elements (Oxygen, Calcium, and Titanium) using Energy Dispersive X-ray Spectroscopy (EDS) technique. In Figure 9(a), the calcined sample is observed optically, showing changes in color and texture due to

© 2025 The Authors.

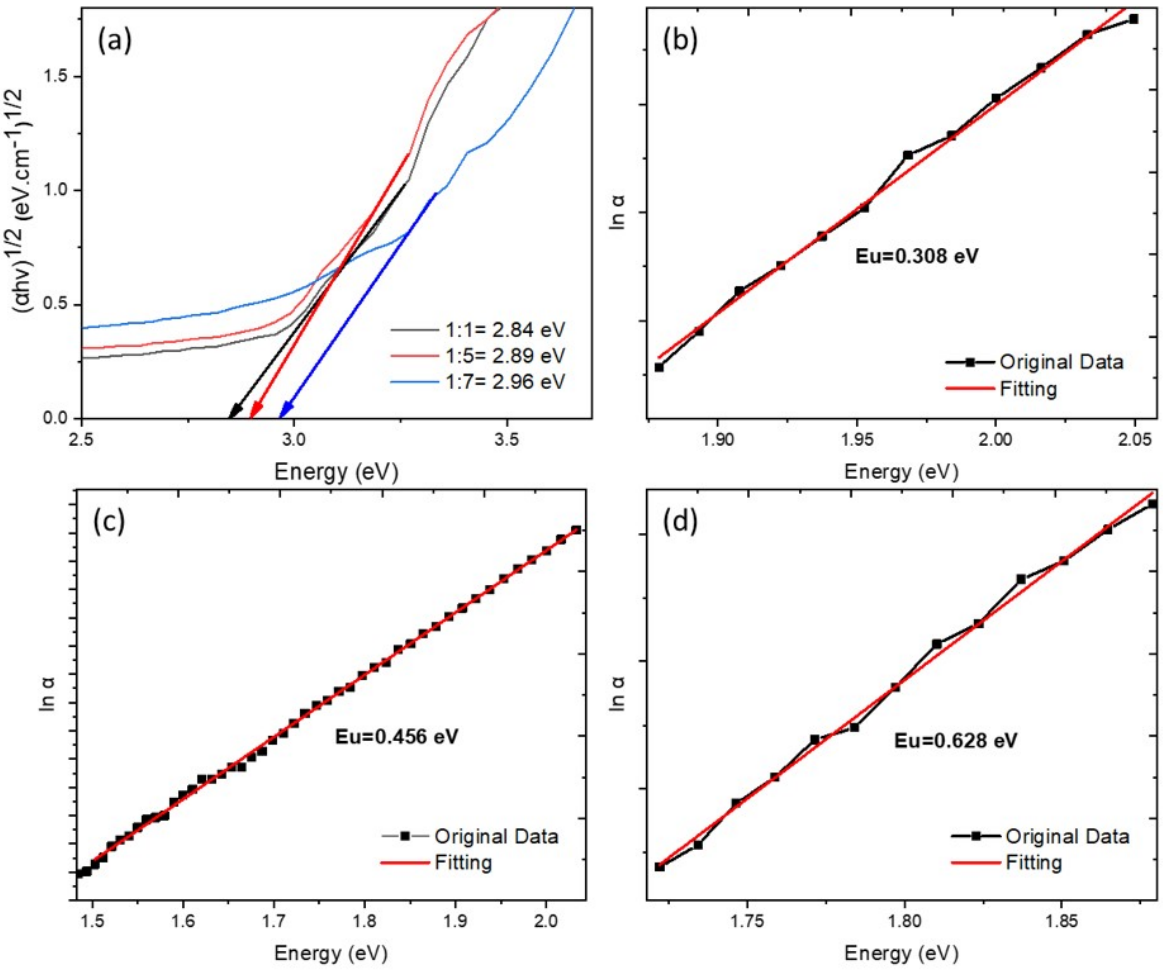

Figure 13. Tauc Plot based on Equation (a) Tauc Plot, and (b-d) (d) Determination of Urbach Energy (E_u) of $TiO_2/CaTiO_3$ Perovskite Composite

high heating. This phenomenon is in line with the research of García-Mendoza et al. (2023), which states that calcination can cause phase transitions and chemical reactions between precursors, thus affecting the visual characteristics of the material. The particle size distribution graph in Figure 9(b) shows a particle size distribution pattern of 21.23 μm. This result is slightly different from the XRD calculation due to differences in measurement methods. However, the large crystallite size obtained also strengthens the results that the particle size of the $TiO_2/CaTiO_3$ perovskite composite tends to be high. This indicates that the growth of $CaTiO_3$ crystallites is influenced by the kinetics of nucleation and particle growth, as reported by Novianti et al. (2022). Meanwhile, the element mapping in Figure 9(c), Figure 9(d), and Figure 9(e) shows the distribution of the main elements in the material.

Figure 9(c) shows a uniform distribution of Oxygen (O) throughout the area, indicating the presence of oxides in the structure. Figure 9(d) displays a fairly wide distribution of Calcium (Ca), indicating the involvement of this element in the formation of the $CaTiO_3$ perovskite phase. Meanwhile, Figure 9(e) shows a high concentration of Titanium (Ti) elements in some areas, which may indicate the presence of residual TiO_2 phases or Ti-rich domains. These mapping results are in accordance with the research of Saputra et al. (2024), who found that in the synthesis of $CaTiO_3$-based perovskites, the distribution of elements is often not homogeneous, especially if there are still residual precursors that have not reacted completely.

Figure 10 shows the EDS spectrum results of $TiO_2/CaTiO_3$ material, which is used to analyze the elemental composition of the sample after calcination at 900°C. This spectrum displays characteristic peaks of the main constituent elements, namely O, Ca, and Ti, indicating the presence of the $TiO_2/CaTiO_3$ perovskite phase. The dominant Ti−K peak indicates that Titanium is the main component in the material structure, while the Ca−K and O−K peaks confirm the presence of $CaTiO_3$ as the main phase. The percentage of $TiO_2/CaTiO_3$ elemental

© 2025 The Authors.

composition can be seen in Table 5.

Based on Table 5, Ti element has the highest mass percentage, which is 61.30% with an atomic percentage of 36.22%. O is present with a mass percentage of 34.30% and the highest atomic percentage of 60.68%, indicating its involvement in the formation of oxides in the material. Meanwhile, Ca has a lower mass percentage, which is 4.39%, with an atomic percentage of 3.10%. These results are in line with the perovskite structure of $TiO_2/CaTiO_3$, where Ti is more dominant than Ca, and indicate that the synthesized material has an element ratio that is in accordance with its theoretical composition. Furthermore, the BET test results can be seen in Figure 11.

Figure 11 shows the results of surface texture characterization of $TiO_2/CaTiO_3$ perovskite composites that have been calcined at 900°C using the BET method. Figure 11(a) shows the nitrogen adsorption-desorption isotherm curve that forms a Type IV isotherm pattern with the presence of a fairly clear hysteresis loop. The characteristic of the Type IV isotherm is the presence of multilayer adsorption and capillary condensation phenomena that occur in the mesoporous pores. The hysteresis loop indicates that the adsorbed nitrogen is not immediately released during the desorption process, which usually occurs in materials with open or incohesive cylindrical pore structures. This indicates that the material has a stable mesoporous structure and does not collapse during the adsorption process. Figure 11(b) strengthens this conclusion through the pore size distribution based on the BJH (Barrett–Joyner–Halenda) method, both in adsorption and desorption data. The distribution peaks are in the range of 3-5 nm, which directly classifies the material as mesoporous, according to the IUPAC definition. The higher pore volume in the desorption data compared to the adsorption is due to the phenomenon of nitrogen being retained in small or narrow pores during desorption, so that it is not released immediately, and creates a cumulative volume difference. This phenomenon is common in materials with incohesive or branched pore structures, which can hinder the backflow of gas.

Figure 11(c) shows the linear plot of the BET equation, which is used to calculate the monolayer volume (Vm) and specific surface area (SSA). The excellent linearity (R^2 = 0.99) indicates that the basic assumptions of the BET model-such as the formation of a monolayer before a multilayer, and the absence of lateral interactions between gas molecules-are quite satisfied in this material within the relative pressure range used (P/P_0 = 0.05-0.3). This means that the adsorption process takes place in a structured and uniform manner on the material surface, which is an important indication that the material has a reliable active surface for applications such as photocatalysis or gas adsorption. Meanwhile, Figure 11(d) shows the results of t-plot analysis, which is used to separate the contribution of micropore and external surface area (mesopores and macropores). The slope of the linear regression on the adsorption data (1.018) and desorption (0.989) with high determination coefficients (0.93 and 0.97, respectively) indicates that the specific surface formed is predominantly derived from mesopores, not micropores.

This indicates that during the synthesis and calcination process, no significant micropore structure was formed-which could have been closed or collapsed at high temperatures. In addition, the slope approaching one also indicates that the solid surface is relatively homogeneous, without any areas with selective adsorption or very dominant active sites. Overall, these characterization results indicate that the $TiO_2/CaTiO_3$ composite calcined at high temperatures is able to maintain a stable mesoporous structure, has sufficient surface area to support reactivity, and a uniform pore distribution. These findings are in line with the study by Khezami (2023), who reported that mesoporous silica-based materials exhibited Type IV isotherms with pore sizes in the range of 3–6 nm and similar hysteresis loops, indicating a good open-pore structure. Similarly, a study by Bhat et al. (2024) on activated carbon from biomass also showed a t-plot pattern that was close to linear, indicating the dominance of mesopores without significant micropore contribution. These results confirm that the formed mesoporous structure is not only stable at high temperatures but can also enhance the diffusion capacity of molecules, which is very important in applications such as photocatalysis, pollutant adsorption, or energy storage systems.

3.5 Absorbance Characteristics of $TiO_2/CaTiO_3$ Perovskite Composites

Testing of the optical properties of the $TiO_2/CaTiO_3$ perovskite composite material was carried out using a UV-Vis spectrophotometer, the absorbance value of which can be seen in Figure 12 with the wavelength used ranging from 200 nm to 1100 nm. Figure 12 shows the UV-VIS characterization results of $TiO_2/CaTiO_3$ perovskite composites with variations in the mass ratio of TiO_2 and $CaCO_3$ (1:1, 1:5, and 1:7). The reflectance graph in Figure 12(a) shows that the higher the $CaCO_3$ content, the higher the reflectance, especially in the shorter wavelength region (320-390 nm wavelength). This indicates changes in the optical properties of the material due to differences in the precursor ratio, which can affect the crystal structure and morphology of the particles formed. Meanwhile, the absorbance graph in Figure 12(b-d) shows the deconvolution of the absorbance spectrum using the peak fitting method, which identifies two main absorbance peaks. The first more dominant peak (marked in red) indicates the main electronic transition of $CaTiO_3$, while the second peak (in green) can be attributed to the contribution of secondary phases or structural defects in the material. Increasing the TiO_2 ratio causes a small shift in the position of the absorbance peak, indicating variations in the degree of crystallinity or particle size distribution. The shift in wavelength from 348 nm, 339 nm, to 327 nm with increasing TiO_2 ratio indicates a change in the electronic structure and optical properties of the material.

The shift towards a smaller wavelength (blueshift) is generally associated with an increase in the crystal grain size or a reduction in structural defects in the material. In this case, the addition of higher TiO_2 likely contributes to the increase in the

© 2025 The Authors.

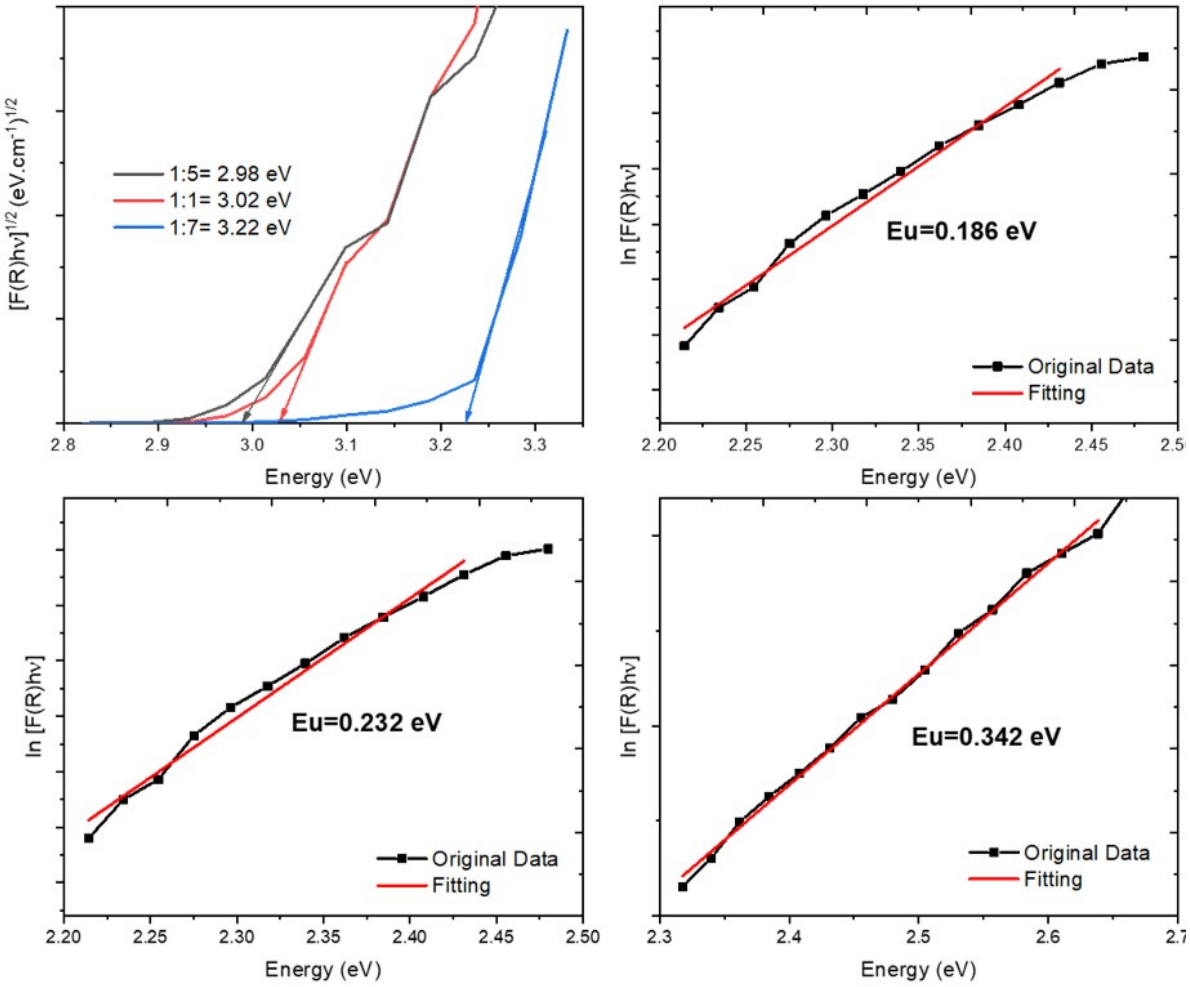

Figure 14. (a) Tauc Plot based on the Kubelka–Munk Equation, and (b-d) Determination of the Urbach Energy (E_u) of $TiO_2/CaTiO_3$ Perovskite Composites

crystallinity of $CaTiO_3$, which causes changes in the electronic transition of the material. Previous studies have shown that the precursor ratio affects the particle size and energy band structure in perovskite materials (Kaabi et al., 2023; Mishra et al., 2024a). It was also found that increasing the TiO_2 content leads to the formation of larger crystal domains and a decrease in the concentration of oxygen defects. This results in a slightly larger bandgap energy shift, so that the main absorption wavelength shifts to a shorter direction. In addition, based on the theory of optical transitions, the blueshift shift can be attributed to the quantum size effect in semiconductor materials, where a smaller grain size causes an increase in exciton energy. In this case, if the increase in TiO_2 causes a decrease in the grain or particle size, then the increase in the energy bandgap leading to the blueshift is a natural effect.

Compared with previous studies, these results are in line with studies showing that increasing calcium in the synthesis of $CaTiO_3$ can cause an increase in reflectance due to the formation of secondary phases such as CaO or $Ca(OH)_2$, which have an effect on the optical properties of the material. Several studies have also reported that the energy bandgap of $CaTiO_3$ can vary slightly depending on the synthesis method and calcination conditions, which can affect the distribution of absorbance peaks. Furthermore, the energy bandgap calculation of the $TiO_2/CaTiO_3$ perovskite composite has been carried out which is determined by the Tauc plot, Kubelka-Munk (Yang and Kruse, 2004), and Urbach Energy (E_u) methods (Ledinsky et al., 2019) (see Figure 13 and Figure 14). The calculation of the bandgap energy by the Tauc plot method is determined by drawing a straight line in the linear region of the relationship graph between ahv1/2 and hv, until the energy bandgap value is obtained.

The Urbach energy (E_u) is determined, which originates from the states located in the band gap, which is related to the disorder in the structure and is given as $\alpha = \alpha_0\ exp(hv/E_u)$, where α is the absorption coefficient proportional to F(R), hv

© 2025 The Authors.

is the photon energy, and (E_u) is the Urbach energy. The calculation of the Urbach energy is done by two methods, first the Tauc curve transformation and second the Kubelka–Munk curve transformation. The inverse of the slope of the linear part of this curve, Figure 13(b-d), which is observed below the optical band gap, will be equal to the value of E_u. The Urbach energy from the absorption results which are then calculated using the Tauc equation has values of 0.308 eV, 0.456 eV, and 0.628 eV, which indicate a larger disorder in the structure and/or a larger contribution from defects to the states located in the band gap. These results confirm that the higher the energy gap of $TiO_2/CaTiO_3$ perovskite due to absorption, the higher the Urbach energy.

Furthermore, the energy gap calculation is carried out using the reflectance results formed using the Kubelka–Munk function, by plotting $ln[F(R)]$ against hv. The results can be seen in Figure 14.

Figure 14(a) shows that increasing the ratio of TiO_2 in the composite results in an increase in the band gap energy, with values of 2.98 eV (1:5), 3.02 eV (1:1), and 3.22 eV (1:7), respectively. This shift indicates that increasing the TiO_2 content in the composite causes band gap expansion, which can be attributed to the quantum effect of size or changes in the electronic structure of the material. The calculation results using reflectance are slightly higher than absorption, but these results are still within normal limits based on Sen et al. (2022). Figure 14(b-d) illustrates that the Urbach energy increases with increasing gap energy. These results are in line with previous studies showing that the band gap energy of TiO_2-based materials increases significantly with the presence of other composite materials.

A study by Ezat et al. (2021) showed that doping $CaTiO_3$ on TiO_2 can increase the band gap due to changes in the electronic structure and the formation of smaller crystal domains. In addition, a study by García-Mendoza et al. (2023) also reported that increasing TiO_2 content in perovskite systems can cause a blueshift effect on the optical absorption spectrum, which is in line with the trend observed in this study.

4. CONCLUSIONS

This study successfully synthesized $TiO_2/CaTiO_3$ perovskite composites using calcium carbonate ($CaCO_3$) from Pinctada maxima shell waste. The synthesis results showed that the color of the resulting powder varied depending on the calcination temperature, where the sample calcined at 900°C had the whitest color, indicating a more perfect formation of $CaTiO_3$. FTIR analysis confirmed the presence of main functional groups such as Ca−O, Ti−O, C−O, and O−H, indicating the successful synthesis of $TiO_2/CaTiO_3$ perovskite composites. The DTA-TGA analysis confirms that increasing the calcination temperature from 700°C to 900°C significantly reduces mass loss and thermal events, indicating the progressive elimination of volatiles and organics. The smoother DTA profile at 900°C reflects the formation of a thermally stable, well-crystallized $TiO_2/CaTiO_3$ perovskite structure with minimal residual transformation. XRD analysis showed the presence of the crystalline phase of $CaTiO_3$ as well as the anatase and brookite phases of TiO_2. At a temperature of 700°C, the calcite phase ($CaCO_3$) was still detected, indicating that the decomposition process was not yet complete. The XRD results also showed that the higher the calcination temperature, the particle size obtained also tended to decrease.

The morphology of $TiO_2/CaTiO_3$ perovskite is in the form of agglomerated granules with increasingly uniform particle sizes as the calcination temperature increases. The BET analysis of the $TiO_2/CaTiO_3$ composite calcined at 900°C shows a specific surface area (SSA) of 11.42 m^2/g, with a pore size distribution ranging from 3–5 nm based on BJH analysis. The high correlation coefficient (R^2 = 0.99) in the BET plot and t-plot slopes near 1 confirm the dominance of mesopores and uniform surface characteristics. The results of UV-Vis analysis show that the $TiO_2/CaTiO_3$ perovskite composite has a band gap value that tends to increase when using the tauc curve or the Kubelka-Munk function, indicating a transition to a more dominant $CaTiO_3$ perovskite structure. As a recommendation for further research, it is recommended to conduct further testing of the electrical properties and efficiency of perovskite-based solar cells from $CaTiO_3$ powder. In addition, the homogenization time of the base material should be extended so that the mixing of the two materials can be more optimal.

5. ACKNOWLEDGEMENT

This research was funded by the 2023 fiscal year Internal Fund Grant of the University of Mataram through the Senior Lecturer Acceleration Research Scheme under contract number 2536/UN18.L1/PP/2024 in the name of Dian W. Kurniawidi. We would also like to express our sincere appreciation to Nonik Septiani and Mustika, undergraduate students from the Department of Physics, Faculty of Mathematics and Natural Sciences, University of Mataram, for their technical assistance during the laboratory activities. Our gratitude is also extended to the Research Center for Biomass and Bioproducts, National Research and Innovation Agency (BRIN), West Java, 16911, Indonesia, for facilitating the TGA and BET analyses.

REFERENCES

Aftabuzzaman, M., C. Lu, and H. K. Kim (2020). Recent Progress on Nanostructured Carbon-Based Counter/Back Electrodes for High-Performance Dye-Sensitized and Perovskite Solar Cells. *Nanoscale*, **12**(34); 17590–17648

Altin, I. (2023). Perovskite Type B-$CaTiO_3$ Coupled with Graphene Oxide as Efficient Bifunctional Composites for Environmental Remediation. *Processes*, **11**(11); 11

Attou, L., A. Al-Shami, J. Boujemaâ, O. Mounkachi, and H. Ez-Zahraouy (2022). Predicting the Structural, Optoelectronic, Dynamical Stability and Transport Properties of Boron-Doped $CaTiO_3$: DFT Based Study. *Physica Scripta*, **97**(11); 115808

Beuvier, T., Y. Chushkin, F. Zontone, A. Gibaud, O. Cherkas,

© 2025 The Authors.

J. D. Silva, and I. Snigireva (2022). Self-Transformation of Solid $CaCO_3$ Microspheres into Core-Shell and Hollow Hierarchical Structures Revealed by Coherent X-Ray Diffraction Imaging. *IUCrJ*, **9**(5); 580–593

Bhat, D. K., H. Bantawal, P. I. Uma, S. P. Kumar, and U. S. Shenoy (2024). Designing Sustainable Porous Graphene-$CaTiO_3$ Nanocomposite for Environmental Remediation. *Sustainable Chemistry for the Environment*, **5**; 100071

Cerón-Urbano, L., C. J. Aguilar, J. E. Diosa, and E. Mosquera-Vargas (2023). Nanoparticles of the Perovskite-Structure $CaTiO_3$ System: The Synthesis, Characterization, and Evaluation of Its Photocatalytic Capacity to Degrade Emerging Pollutants. *Nanomaterials*, **13**(22); 22

Cesconeto, F. R., M. Borlaf, M. I. Nieto, A. P. N. de Oliveira, and R. Moreno (2018). Synthesis of $CaTiO_3$ and $CaTiO_3/TiO_2$ Nanoparticulate Compounds through Ca^{2+}/TiO_2 Colloidal Sols: Structural and Photocatalytic Characterization. *Ceramics International*, **44**(1); 301–309

Chilakala, R., C. Thannaree, E. J. Shin, T. Thenepalli, and J. W. Ahn (2019). Sustainable Solutions for Oyster Shell Waste Recycling in Thailand and the Philippines. *Recycling*, **4**(3); 3

Dassouki, K., S. Dasgupta, E. Dumas, and N. Steunou (2023). Interfacing Metal Organic Frameworks with Polymers or Carbon-Based Materials: From Simple to Hierarchical Porous and Nanostructured Composites. *Chemical Science*, **14**(45); 12898–12925

Diningsih, C. and L. Rohmawati (2022). Synthesis of Calcium Carbonate ($CaCO_3$) from Eggshell by Calcination Method. *Indonesian Physical Review*, **5**(3); 208–215

Ezat, G. S., S. A. Hussen, and S. B. Aziz (2021). Structure and Optical Properties of Nanocomposites Based on Polystyrene (PS) and Calcium Titanate ($CaTiO_3$) Perovskite Nanoparticles. *Optik*, **241**; 166963

Ferrari, A. M., T. O. Germiniano, J. E. Savoia, R. G. Marques, V. A. dos S. Ribeiro, and A. C. Ueda (2019). $CaTiO_3$ Perovskite in the Photocatalysis of Textile Wastewater. *Revista Ambiente & Água*, **14**; e2336

García-Mendoza, M. F., R. Torres-Ricárdez, E. Ramírez-Morales, J. G. Álvarez-Ramirez, L. L. Díaz-Flores, E. del Ángel-Meraz, L. Rojas-Blanco, and G. Pérez-Hernández (2023). $CaTiO_3$ Perovskite Synthetized by Chemical Route at Low Temperatures for Application as a Photocatalyst for the Degradation of Methylene Blue. *Journal of Materials Science: Materials in Electronics*, **34**(10); 873

Giannouli, M. (2021). Current Status of Emerging PV Technologies: A Comparative Study of Dye-Sensitized, Organic, and Perovskite Solar Cells. *International Journal of Photoenergy*, **2021**(1); 6692858

Hamzah, M. S. and B. Nababan (2011). The Effect of Seasons and Depths on Growth and Survival Rate of Pearl Oyster (*Pinctada maxima*) in Kodek Bay, North Lombok. *Jurnal Ilmu Dan Teknologi Kelautan Tropis*, **3**(2); 2

Han, C., J. Liu, W. Yang, Q. Wu, H. Yang, and X. Xue (2017). Photocatalytic Activity of $CaTiO_3$ Synthesized by Solid State, Sol–Gel and Hydrothermal Methods. *Journal of Sol-Gel Science and Technology*, **81**(3); 806–813

Handayana, I. G. N. Y., D. W. Kurniawidi, S. Rahayu, and N. Rahmawati (2022). Characteristics of Calcium Oxide from Pearl Shells (*Pinctada maxima*) Based on Calcination Temperature. *KONSTAN - JURNAL FISIKA DAN PENDIDIKAN FISIKA*, **7**(1); 1

Jabbarzare, S. (2022). Synthesis and Characterization of Ni-Doped $CaTiO_3$ Nano-Powders and Their Potential for the Removal of Cd from Wastewaters. *Journal of Particle Science and Technology*, **8**(1); 9–16

Jiang, Q., G. Li, X. Wang, H. Kang, Z. Chen, E. Guo, and T. Wang (2024). Enhanced Thermoelectric Properties for Eco-Friendly $CaTiO_3$ by Band Sharpening and Atomic-Scale Defect Phonon Scattering. *Materials Today Energy*, **44**; 101655

Kaabi, F. S. A., M. A. Abdulkareem, and N. A. Muhsin (2023). Determining the Optimal Conditions for the Synthesis Nano $CaTiO_3$ Square Prepared from Natural Dolomite Rocks. *Results in Chemistry*, **5**; 100915

Kandiah, K. K., V. Balakrishnan, A. Syafiq, N. A. Rahim, A. K. Pandey, Y. S. Tan, S. J. Dhoble, R. Kasi, and R. Subramaniam (2023). Study on Photoluminescence of Integrated Nano-Calcium Carbonate ($CaCO_3$) Enhanced with Dysprosium (Dy) Doped Calcium Borophosphate (CBP) Phosphor. *Pigment & Resin Technology*, **54**(1); 87–97

Khezami, L. (2023). Remediation of Heavy Metals from Water Using $CaTiO_3$@g-C_3N_4 Nanocomposite as Adsorbent: Synthesis, Performance, Kinetic Modeling and Mechanistic Insights. *Diamond and Related Materials*, **136**; 109996

Kurniawidi, D. W., S. Alaa, E. Nurhaliza, D. O. Safitri, S. Rahayu, M. Ali, and M. Amin (2022). Synthesis and Characterization of Nano Chitosan from Vannamei Shrimp Shell (*Litopenaeus vannamei*). *Jurnal Ilmiah Perikanan Dan Kelautan*, **14**(2); 2

Kurniawidi, D. W., G. Alawiyah, S. Rahayu, Masruroh, R. Wirawan, A. S. Destrianingtyas, N. Septiani, T. Ardianto, and R. R. Illahi (2024). Modification of Chitosan Isolation Method from Pearl Oyster Shell (*Pinctada maxima* sp) as a Source of Natural Polymer. In *Journal of Physics: Conference Series*, volume 2866. page 012015

Lalan, V., V. P. M. Pillai, and K. G. Gopchandran (2022). Enhanced Electron Transfer Due to rGO Makes Ag–$CaTiO_3$@rGO a Promising Plasmonic Photocatalyst. *Journal of Science: Advanced Materials and Devices*, **7**(3); 100468

Ledinsky, M., T. Schönfeldová, J. Holovský, E. Aydin, Z. Hájková, L. Landová, N. Neyková, A. Fejfar, and S. D. Wolf (2019). Temperature Dependence of the Urbach Energy in Lead Iodide Perovskites. *The Journal of Physical Chemistry Letters*, **10**(6); 1368–1373

Li, J., Y. Wang, X. Yang, H. Kang, Z. Cao, X. Jiang, Z. Chen, E. Guo, and T. Wang (2022). Processing Bulk Insulating $CaTiO_3$ into a High-Performance Thermoelectric Material. *Chemical Engineering Journal*, **428**; 131121

Li, J., H. Wu, R. Zhong, Y. Wang, S. Ye, H. Zhao, K. Yan,

© 2025 The Authors.

Y. Zhu, Z. Hu, W. Xie, and T. Zhang (2024). Quenching-Induced Oxygen Vacancy Engineering Boosts Photocatalytic Activities of $CaTiO_3$. *Applied Surface Science*, **670**; 160619

Liu, G., B. Yang, H. Chen, Y. Zhao, H. Xie, Y. Yuan, Y. Gao, and C. Zhou (2019). In Situ Surface Modification of TiO_2 by $CaTiO_3$ to Improve the UV Stability and Power Conversion Efficiency of Perovskite Solar Cells. *Applied Physics Letters*, **115**(21); 213501

Mishra, S., R. Dom, and B. Sundaram (2024a). Effect of Operating Parameters on Photocatalytic Treatment of Synthetic Wastewater Using $CaTiO_3$. *Applied Environmental Research*, **46**(3); 3

Mishra, S., P. K. Naini, and B. Sundaram (2024b). Effect of Calcination Temperature on Structural, Optical and Photocatalytic Properties of Calcium Titanate ($CaTiO_3$) Nanoparticle. *Results in Optics*, **16**; 100676

Novianti, D. R., F. Haikal, U. A. Rouf, A. Hardian, and A. Prasetyo (2022). Synthesis and Characterization of Fe-Doped $CaTiO_3$ Polyhedra Prepared by Molten NaCl Salt. *Science and Technology Indonesia*, **7**(1); 17–21

Saputra, K., M. Masruroh, H. Susanto, and R. Apsari (2024). Tapping into the Power of Sol-Gel Method for Enhanced Antimicrobial Activity of Titania Nanoparticles. *Science and Technology Indonesia*, **9**(3); 546–555

Sen, S., A. Mondal, R. K. Parida, and B. N. Parida (2022). Improved Optical, Dielectric, Impedance, and Magnetic Properties of $(BiFeO_3)\_0.6(CaTiO_3)\_0.4$ for Multifunctional Utilities. *Inorganic Chemistry Communications*, **142**; 109664

Singh, V., A. A. Bhat, A. R. Kadam, S. Saravanakumar, P. K. Tripathi, S. J. Dhoble, and J. B. Joo (2024). Optimal Doping of Ho^{3+} in $CaTiO_3$ Perovskite for Enhanced Photoluminescence and Sustainable Green Emission. *Journal of Electronic Materials*, **53**(10); 6384–6394

Song, Y., J. Wang, X. Chen, S. Yu, R. Ban, X. Yang, X. Zhang, and Y. Han (2022). Study the Effects of Dry-Wet Cycles and Cadmium Pollution on the Mechanical Properties and Microstructure of Red Clay. *Environmental Pollution*, **302**; 119037

Tanos, F., E. Makhoul, A. A. Nada, M. F. Bekheet, E. Petit, A. Razzouk, G. Lesage, M. Cretin, and M. Bechelany (2024). Efficient Peroxymonosulfate Activation by Metallic Copper in TiO_2–$CaTiO_3$–Cu_2O–Cu Anodes for Electrocatalytic Degradation of Organic Pollutants. *Advanced Energy and Sustainability Research*, **5**(10); 2400102

Thomas, K., A. Rahman, A. Khandakar, P. Chelvanathan, B. Aissa, and M. I. Hossain (2025). Optimizing Light Management in Bifacial Perovskite Solar Cells Using Silica-Based Anti-Dust and Anti-Reflection Coatings for Harsh Environments. *Processes*, **13**(2); 2

Vasconcelos, S. J. T., M. A. S. Silva, R. G. M. de Oliveira, M. H. B. Junior, H. D. de Andrade, I. S. Q. Junior, C. Singh, and A. S. B. Sombra (2021). High Thermal Stability and Colossal Permittivity of Novel Solid Solution $LaFeO_3/CaTiO_3$. *Materials Chemistry and Physics*, **257**; 123239

Wendari, T. P., M. A. Akbar, A. F. Izzati, H. Haidar, A. Rizki, Zulhadjri, S. Arief, N. Mufti, and G. R. Blake (2024). Structure, Dielectric, and Energy Storage Properties of Perovskite $CaTiO_3$ Ceramic Synthesized Using the Natural Calcium from Pensi Shell (*Corbicula moltkiana*) Waste. *Journal of Molecular Structure*, **1307**; 137949

Widiastuti, W., S. D. B. Bangun, N. L. Y. Giri, and V. Fahmi (2023). Exploring the Community Structure of Plankton in the Maricultures Sites of Kodek Bay, Lombok Island. *Buletin Oseanografi Marina*, **12**(1); 133–141

Yang, L. and B. Kruse (2004). Revised Kubelka–Munk Theory. I. Theory and Application. *JOSA A*, **21**(10); 1933–1941

© 2025 The Authors.